# UPNM SUBSONIC WIND TUNNEL FLOW MEASUREMENTS TECHNIQUE AND CALIBRATION

Z Methal<sup>1</sup>, Syahin AAT<sup>1</sup>, Rahman MRA<sup>1,2</sup>, Saad MR<sup>1,2\*</sup>

<sup>1</sup>Department of Mechanical Engineering, Faculty of Engineering, Universiti Pertahanan Nasional Malaysia, Kem Perdana Sungai Besi, 57000 Kuala Lumpur, Malaysia <sup>2</sup>Centre for Defence Research and Technology (CODRAT), Universiti Pertahanan Nasional Malaysia, Kem Perdana Sungai Besi, 57000 Kuala Lumpur, Malaysia

### **Article history**

Received: 12 April 2023

Received in revised form: 25 May 2023

Accepted: 27 June 2023

Published online: 30 June

2023

\*Corresponding author: mohdrashdan@gmail.c om

#### **ABSTRACT**

A common fundamental tool used for aerodynamic testing is the wind tunnel. With this decent instrumentation, many researchers are able to come up with trustworthy and prospective data to simulate various kinds of applications, including low Reynolds number applications. However, the topic of the calibration technique of aerodynamic instruments for wind tunnels has not been thoroughly discussed for the user's proper guidance before the experiment is conducted. Therefore, this paper will explain the method of wind tunnel calibration and the flow measurement technique that is specific to subsonic flow, open loop, and suction-type wind tunnels. The wind tunnel is the property of UPNM, with a test section dimension of 1 m length, 0.3 m height, and 0.3 m width and capable of running up to 100 m/s. Based on the calibration results, the accuracy in the measurement of pressure using Scanivalve is 0.9%. For force balance, the accuracy of lift and drag forces is 1% for three-component force balance and 0.1% for sting balance. The seeding particles fall within the acceptable range based on two consecutive image frames, the particle density, and the correlation value during PIV calibration. The average measurement of turbulence intensity is 1.4% for low speeds and 0.2% for high speeds. This confirms a decent instrumentation condition and the correctness of the data reduction algorithm.

**Keywords**: Subsonic Wind Tunnel, Particle Image Velocimetry (PIV), Flow Measurement, Flow Measurement Technique, Calibration

### 1.0 INTRODUCTION

The intricacy of flow through the solid object has opened significant contributory factors to the development of advanced tools like computational fluid dynamics (CFD). CFD has increased



significantly in a wide area of disciplines and industries, including aerospace, automotive and power generation. The capabilities of CFD in processing complex geometry model, rebuilding boundary layer condition in real world while generating high accuracy and better understanding of flow physics with outstanding performance at relatively low cost has become more practical, perceptive, and achievable. Besides, CFD is capable of generating precise calculation parameters including pressure range contour [1], vorticity [2], velocity [3], temperature [4] and visualize fluid motion through objects [5]. While experimentally often sees insightful, owing to the limitation of resources to conduct experiments, CFD consecutively delivered best practice for broad range of applications. Nonetheless, a few constrains remain. First, CFD is difficult to perform technically and can results in data uncertainties if erroneous modelling methods are applied [6][7]. Second, CFD consists of various type of grid and computational domain parameters. Incorrect selection of domain such as the outlet and inlet boundary, mesh topology and refinement and y+ value can significantly increase the calculation loads, thus increasing the simulation time by two times or more [8]. Third, computational method requires considerable capital expenditure including software upgrade, license renewal, PC upgrade and maintenance as well as continuity in-house training, which may dramatically increase the organization expenses [9]. In fact, CFD reliability is strongly dependent on experiment validation especially in design optimization [10]. For that reason, researchers remain with experimental explorations to obtain detailed results and to make final decisions for large number of engineering applications.

A fundamental tool for testing aerodynamics experiment is wind tunnel. Wind tunnel consists of four basic types: subsonic, transonic, supersonic, and hypersonic. These types are classified based on the amount of speed in test section relative to the speed of sound which is denoted as Mach number (M) [11]. The working section can be divided into two primary types: open and closed-circuit. For open-circuit, both ends are opened, and the air draws from the room into the test section [12]. Meanwhile, for closed-circuit, the air draws from the exit of the fan to the contraction section and return to the test section [13]. Open-circuit wind tunnel is well-known for its low-cost construction and convenient for smoke visualization [14] and oil flow visualization [15]. Nevertheless, the operating cost for open-circuit tunnel is considerably higher than closed-circuit. In terms of flow quality, closed-circuit is exceptional in providing uniform flow in the test section compared to open-circuit as it equipped with corner turning vanes and screens [10].

The scale of wind tunnel varies depending on the application. Some wind tunnel can hold models as big as the size of real airplane while some are small enough to hold very tiny models. Commonly, in universities, small-scale wind tunnel is the most convenient type for research work of aerodynamic as it offers low operation and construction cost and does not require large spaces in laboratory [16]. Besides, small-scale wind tunnel typically places in the closed building and for that reason it can be seen that closed-circuit will be less effective for return vanes and ducts [17].

Small-scale wind tunnels with open circuit received numerous attentions as a tool of measurement in aerodynamic. Recent work in experimental study has shown growing interest on the application with low Reynolds number (Re) such as unmanned air vehicle (UAV) [18], micro air vehicle (MAV) [19] and micro wind turbine with aimed to study the effect of flow towards the wing, propeller, blades as well as to improve the performance. Jumahadi et al [20]



conducted an experimental study using hybrid flow control consisting of combine active blowing and passive micro-vanes on a wing having NACA 4415 to minimize the flow separation and improved the aerodynamic efficiency up to 33.7% with wind tunnel testing. Earlier, Baljit et al [21] investigated the effect of suction and jet blowing towards boundary layer separation on NACA 0012 and discovered that the suction and jet blowing manage to increase about 30% to 40% of lift-to-drag ratio in comparison with a clean airfoil. In separate study, Felli [22] investigated the effect of propeller blade vortices towards wing during approach, encounter and penetration phases and found that the propeller tip vortices were significantly affected the boundary layer of the wing during encounter and early penetration phase but not showing any significant effect on the whole wing system. In the same vein, Ananda et al [23] found remarkably increase of lift-to-drag ratio as high as 70% compared to clean airfoil when using Wortmann FX 63-137 wing with propeller in tractor configuration. Also, an effort to investigate the capability of micro wind turbine of Savonius and Darrieus in terms of RPM, TSR, CL, CD and CP have been made for various design and configuration by means to increase the power generation capacity at low wind speed condition [24]–[27].

For many years, numerous experiments were performed for aerodynamic study but only a few were discussed on the calibration method. De Almeida et al. [10] and Namirian et al [12] presented the design and construction of subsonic wind tunnels but did not perform the calibration technique well. Several attempts have been made to provide calibration guidelines for wind tunnel measurement but only restricted to the force balance [28][29]. Therefore, this paper aims to study the wind tunnel operating equipment and calibration process for aerodynamic analysis which is limited to force balance, pressure scanner and particle image velocimetry (PIV). Besides, a guideline to measure the turbulent intensity will be discussed in the last section to ensure that the wind tunnel effect is not significant when the experiments are conducted.

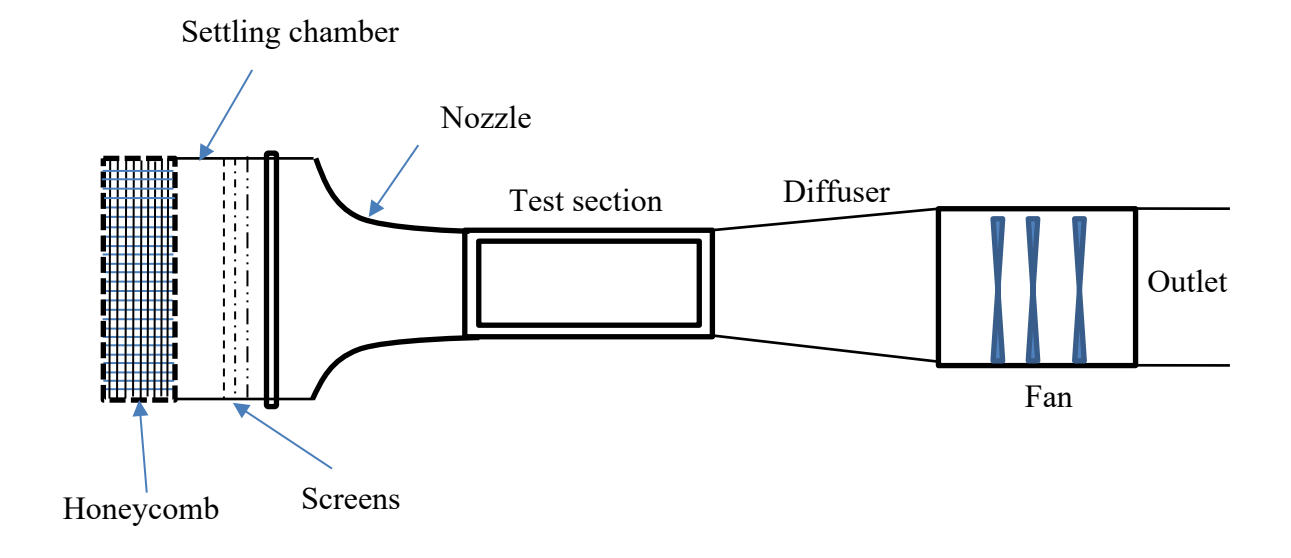


Figure 1: Schematic diagram of open-circuit wind tunnel



# 2.0 METHODOLOGY

#### 2.1 Subsonic Wind Tunnel

The wind tunnel was designed and manufactured by Long Win Science and Technology Corporation and has been installed at Universiti Pertahanan Nasional Malaysia (UPNM) in 2016. The wind tunnel type is open circuit having a speed ranging from 0 to 105 m/s (Mach 0.3). It has a dimension of 1 m (width), 10 m (length) and 2 m (height) over the rough floor. The size of the test section is 0.3 m (width), 0.3 m (length), 1 m (height) with a wall thickness of 10 mm. The main components of wind tunnel composed of honeycomb, settling chamber, screens, contraction, test section, diffuser and fan (see Figure 1). All the components are crucial to ensure the uniformity of flow in the tubular passage [30]. Figure 2 shows the configuration of subsonic open-circuit wind tunnel at UPNM.

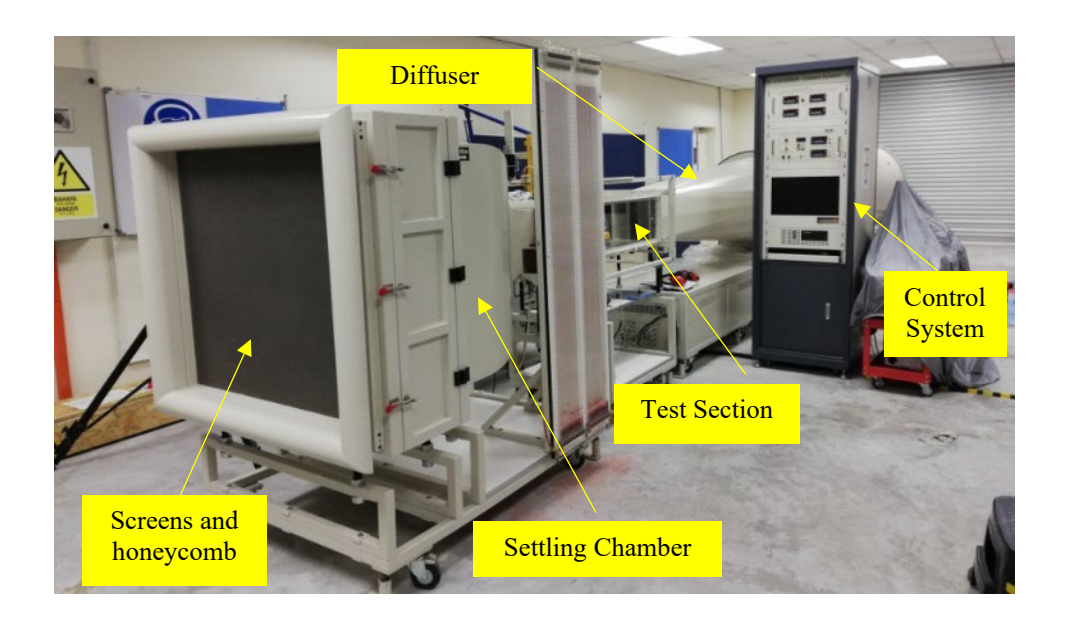
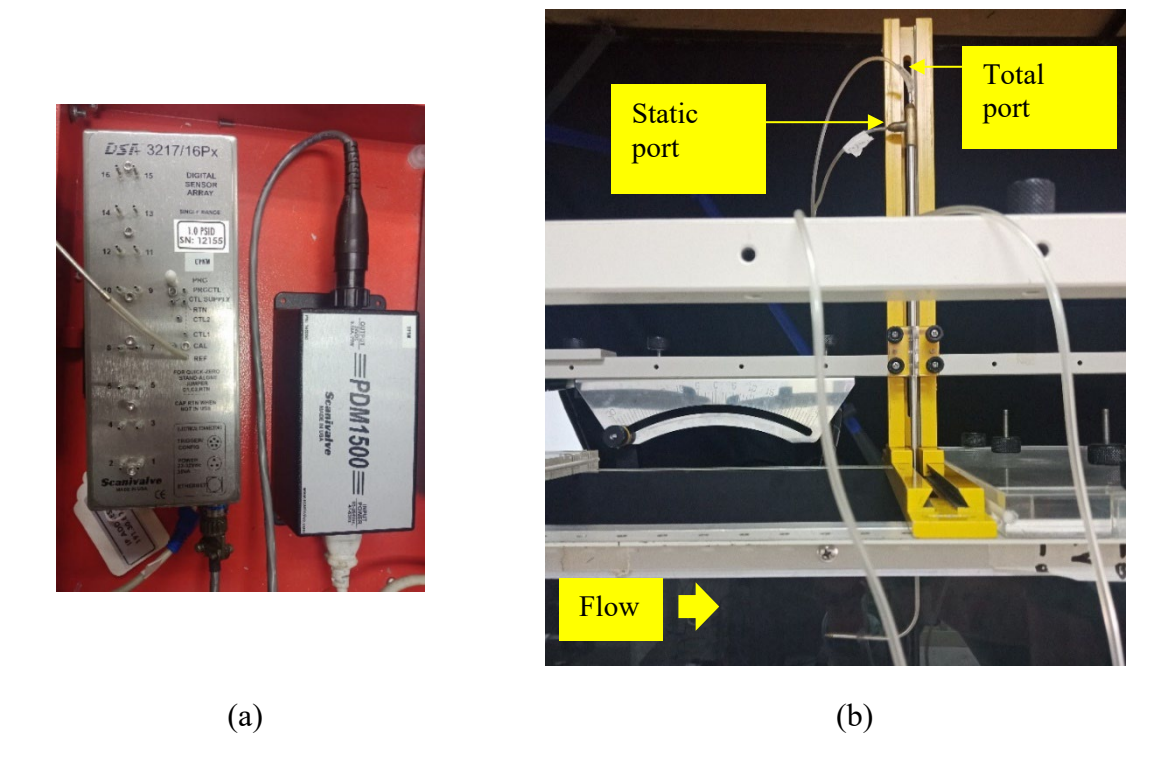


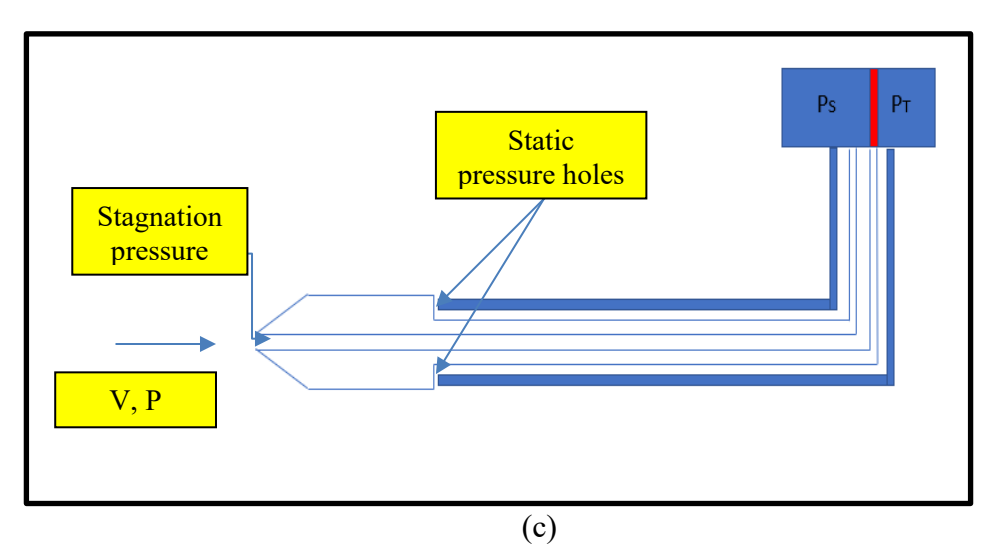


Figure 2: Configuration of subsonic open-circuit suction type wind tunnel



Wind tunnel has powerful multiple fans that create flow far side of the tunnel. The fans are adjustable to achieve a different kind of tunnel speeds and it is controlled by varying the frequency at the control system. For low speed, the speed range is in between 0.5 to 10 m/s. During this condition, only single fan starts spinning. Meanwhile, for high speed (5 to 100 m/s), 3 multiple fans will be running at the same time. The sensitivity of wind tunnel speed is  $\pm 0.25$ % of full-scale range.





**Figure 3:** Velocity measurement with (a) DSA 3217/16Px pressure scanner, (b) Pitot-static probe and (c) schematic diagram



#### 2.2 Wind Tunnel Measurement Instrument: Pressure Measurement

The pressure is measured using a pressure scanner. The model chosen is Scanivalve DSA 3217/16Px as shown in Figure 3(a). The scanner consists of 16 pressure transducer which each of 8 transducers share common calibration valve and reference manifold to generate single reference and calibration port. The measuring range of pressure scanner is 1 psid and can work optimally in high temperature environment between 320F to 1400F. The sensitivity of pressure scanner is  $\pm 0.12\%$  of full-scale range. The National Instrument (NI) data acquisition (DAQ) will be generating different signal for different transducers. NI 9220 data acquisition is selected because it can generate different signal simultaneously in addition to great flexibility of LabView software. To calibrate the pressure scanner (Scanivalve), the measured data will be compared with the pressure chamber. The sensitivity of the pressure is  $\pm 0.1\%$  of full-scale range.

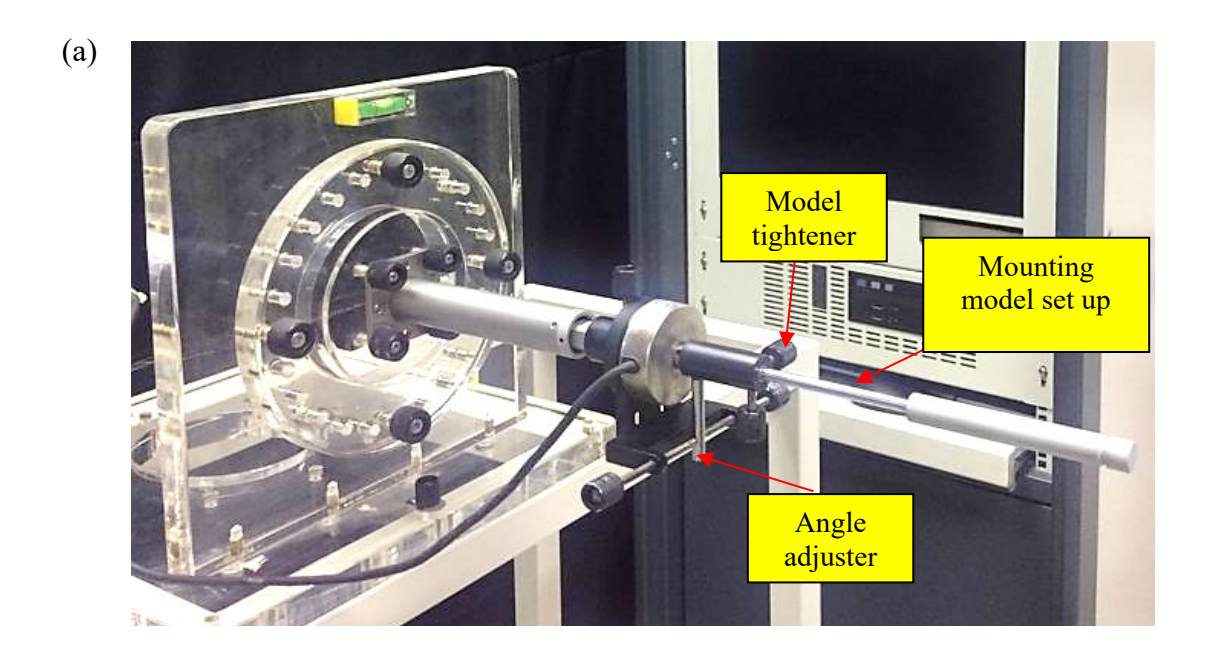
## 2.3 Wind Tunnel Measurement Instrument: Flow Velocity Measurement

Flow measurement is involved in the quantification of fluid motion. The uniformity of flow in the wind tunnel test section is essential for obtaining high-quality results during the experiment. For flow velocity measurement, it is determined based on two measured pressures: static pressure (PS) and total pressure (P0) using a pressure scanner (see Figure 3(a)) connected to the Pitot-static tube (see Figure 3(b)) and pitot rake in the test section of the wind tunnel. The Pitot tube has cylindrical tube with a front hole, having approximately  $\pm 0.2\%$  of full-scale range measurement error (see Figure 3(c) for schematic diagram). Meanwhile for pitot rake, the instrument was customized using 3D printer and the ports was made up of cylindrical steel tube with front hole.

## 2.4 Wind Tunnel Measurement Instrument: Aerodynamic Loads

To describe the condition of aerodynamic loads, the wind tunnel itself is equipped with three-component force balances: axial, normal and moment (see Figure 4(a)). Axial and normal have a maximum load of 5 kg whereas the moment is 1kg.m with the angle adjustment of  $\pm 300$ . The sensitivity of the force balance is 1% of full-scale range, which corresponds to  $\pm 0.3$  N for lift force and  $\pm 0.2$  N for drag force. The magnitude of the measured lift and drag force are found to be within the sensitivity limit of the force balance. To improve the quality of measurement, a recently upgraded force balance with sting type consisting of 5 components is installed, having similar three components in addition to pitching and yawing moment (see Figure 4(b)). The maximum load for axial is 4.5 kg, normal and side force are 11 kg while pitching and yawing moment are 0.5 kg.m. The maximum angle of sting balance is similar to the three-component balances, The accuracy of component loads is improved significantly with 0.1% of full-scale range. NI DAQ will be dominating the signal and sting balance is connected to the same DAQ of the pressure scanner. In the current research, only normal force and axial force will be concentrated.





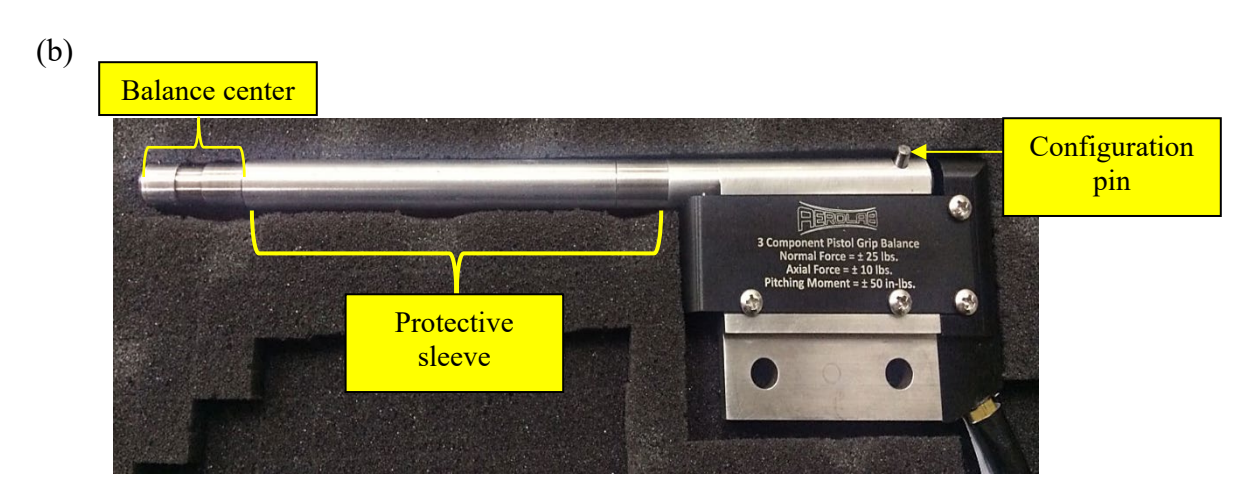


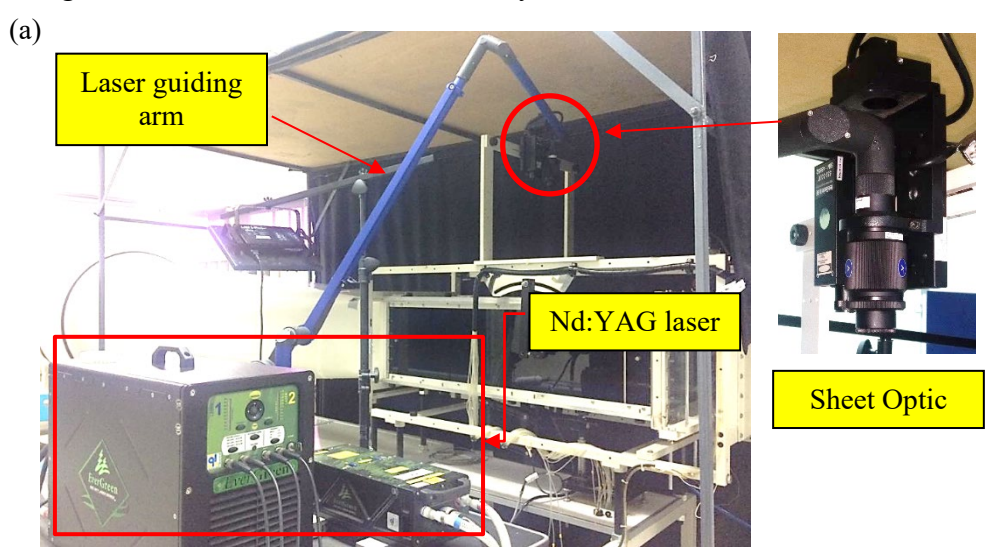
Figure 4: Force Balance with (a) three-components and (b) five components balance

# 2.5 Wind Tunnel Measurement Instrument: Particle Image Velocimetry

Particle Image Velocimetry (PIV) is non-contact optical technique for flow visualization to obtain the velocity field of an entire region within the fluid flow. PIV available for use at the site, comprising of CCD (charge couple device) Imager SX6M camera with single and double frame mode in addition to 2752 x 2200 pixel resolution, high power-double pulsed Neodymiun-doped: Yttrium Aluminum Garnet (Nd:YAG) laser, flexible laser guiding arm, adjustable light sheet optic thickness and interchanging various divergent lenses, aerosol generator and signal processing system. The Imager SX6M camera comes with camera head with USB 3.0 Vision digital image output, power supply, USB 3.0-Vision Cable, Nikon F-mount lens adapter,



trigger adapter, BNC trigger cable and elbow fitting for mounting purpose. In the present PIV system, Quantel Evergreen 200 Nd:YAG laser is used. The laser is double pulsed at 15 Hz with ≤10 ns pulse duration. The laser has a maximum and minimum power output of 135 µs and 400 µs, respectively for the fundamental wavelength of 1064 nm. The laser generates energy output of 0.2 J/pulse, producing 20 MW peak pulse with pulse duration of ≤10 ns. With high intensity pulse, it will produce green color laser light at 532 nm from an infrared light at 1064 nm frequency efficiency for better PIV visualization [31]. Figure 5 below shows PIV arrangement in the wind tunnel laboratory.



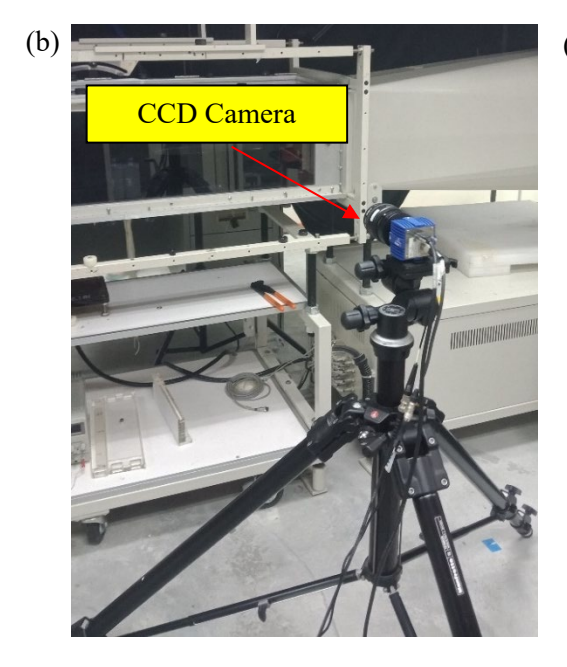




Figure 5: PIV arrangement and measurement tools



#### 3.0 CALIBRATING THE MEASUREMENT SYSTEM

#### 3.1 Pressure Calibration

The instrument used to measure the pressure is Scanivalve. To ensure the accuracy of a pressure measurement devices, a comparison between known measurement from pressure chamber is compared with Scanivalve. The arrangement of the calibration setup is shown in Figure 6.

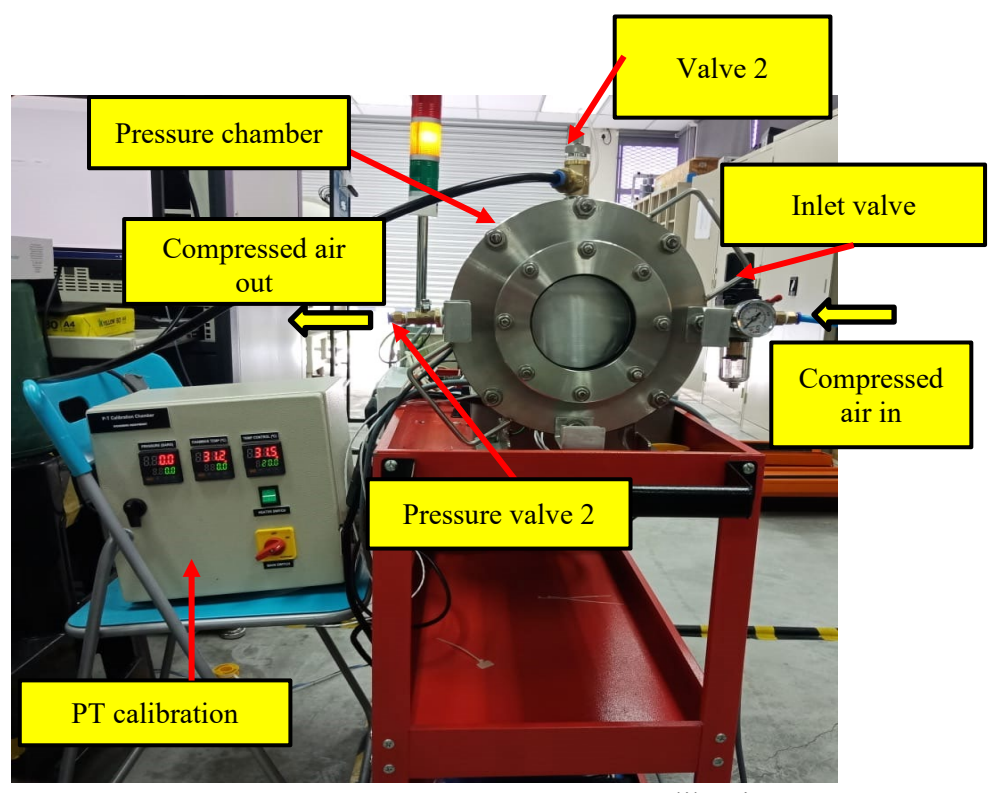


Figure 6: Pressure measurement calibration

The pressure calibration method was shown in Figure 6. The pressurized air was supplied to the pressure chamber through the inlet valve. PT calibration assists to identify the amount of pressurized air inside the pressure chamber. To accommodate with Scanivalve measuring range which is 1 psid, the pressurized air in the chamber was set below 0.1 bar and released steadily to avoid overpressure. The results were captured after 5 minutes, and the graph was plotted to determine the relationship between the Scanivalve against the pressure chamber.

## 3.2 Flow Velocity Calibration

As described previously in section 2.3, the simple measurement of velocity can be obtained by measuring the total pressure and static pressure in the wind tunnel. This relation can be defined as follows:

$$V = \sqrt{\frac{2(P_0 - P_S)}{\rho}} \tag{1}$$



The measurement of pressures in the test section wind tunnel was obtained using handcrafted pitot rake and pitot probe. For pitot rake, it is made up of 3D printer with 16 holes aligned vertically. A steel tube consists of 3.8 mm length and 1 mm diameter was inserted into the holes as a port of silicone tube (see Figure 7 (a)). All 16 ports were connected to pressure scanner to measure the P0 (Figure 7 (b)). For static pressure measurement, Pitot-static probe is available in site and silicone tube will be connected to static port as well as pressure scanner to obtain the reading. Experimental data were projected at frontal, middle and back field in the test section with different selected location and subjected to different wind speed between 11 to 33 m/s after considering the range of velocity that will be used in the future study. The setup of P0 and Ps were shown in Figure 7.

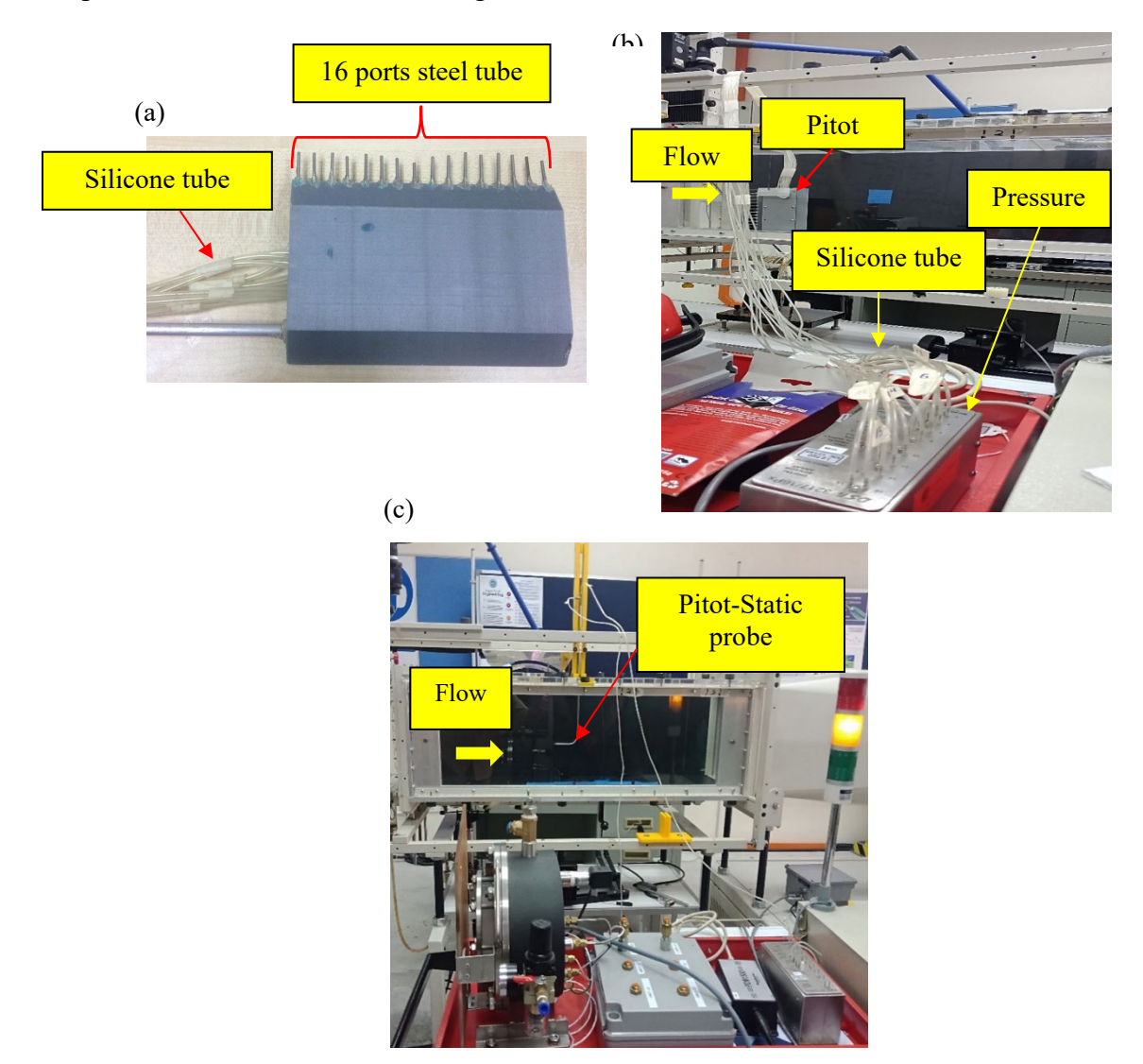


**Figure 7:** Velocity measurement set-up using P<sub>0</sub> and Ps

#### 3.3 Force Balance Calibration

A range of three and five-component balances (sting balance) are available in the wind tunnel,



but only axial and normal components are used. Calibrated weights are applied as a force generator to determine the output signal of the two components. To calibrate the normal component force for each balance, the reference weight is applied at the moment center mounted on the calibration platform and sting support (see Figure 8(a) and (b)). Meanwhile for axial component force, the weight is applied towards the gravity direction (see Figure 9 (a) and (b)). The output signal for these two components (normal and axial) are plotted against the applied load. For measuring the angle of attack (AOA), mini digital protractor is used. The accuracy of mini digital protector is  $\pm 0.40^{\circ}$  of full-scale range. The output signal from the mini digital protractor is plotted against the measured AOA.

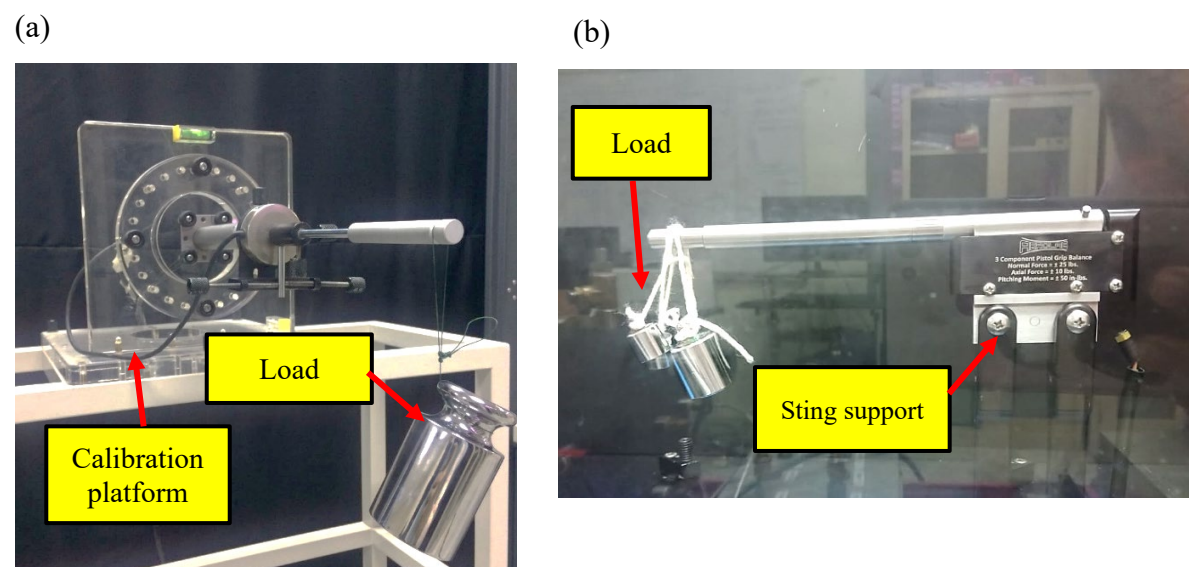


Figure 8: Normal force calibration for (a) three-components and (b) five-components balance

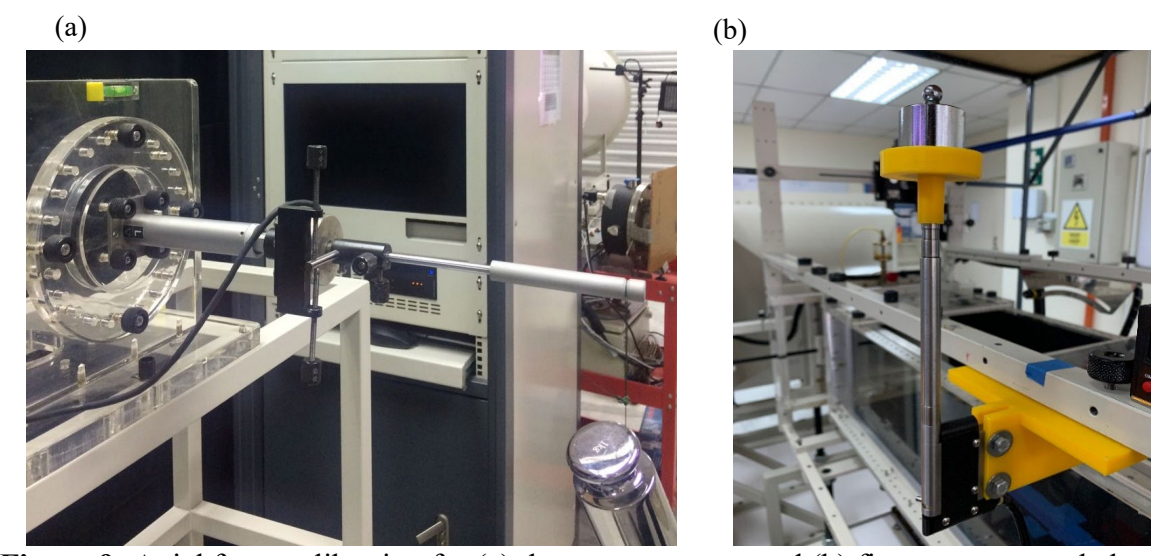


Figure 9: Axial force calibration for (a) three-components and (b) five-components balance



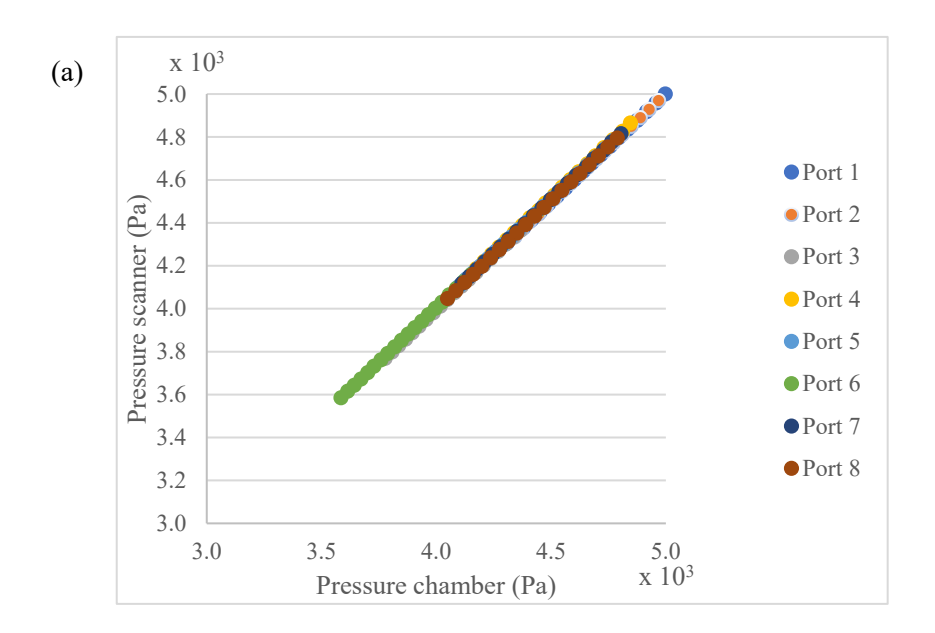
# 3.4 Particle Image Velocimetry (PIV) Calibration

To quantify the velocity fields with great visualization, the size of the seeding particles should be small enough to be a flow tracer and big enough to disperse adequate light for imaging [31]. In this lab, the seeding particle used is di-Ethylhexyl sebacate (DEHS). DEHS can generate better seeding fluid with bigger size of poly-disperse particle. The mean particle diameter is 20 µm with a specific density of 0.9 g/cm3 which is close to water. With Lavision aerosol generator pairing up with DEHS, strong scattered light can be obtained. In addition to generate decent velocity information, the time delay between two consecutive image frames that yielded particle displacement should be in the range of 8 to 10 pixels [32]. Also, the particle density should be under moderate seeding density of 0.05 to reduce the ghost particle that can affect the velocity information [33]. In terms of correlation value, the center of the correlation plane should be higher than all other peaks within the search area otherwise the vector selection is invalid [34]. Therefore, it is suggested to start with large multi-pass window if strong out of plane effects are noticeable so that the invalid vector can be eliminated.

#### 4.0 CALIBRATION RESULTS

#### **4.1 Pressure Measurement**

Figure 10 indicates the relationship between the pressure scanner and the pressure chamber. It is shown that the measured pressure from pressure scanner is nearly close to the value of pressure chamber for all the 16 channels. The percentage difference is about  $\pm 0.1\%$ .





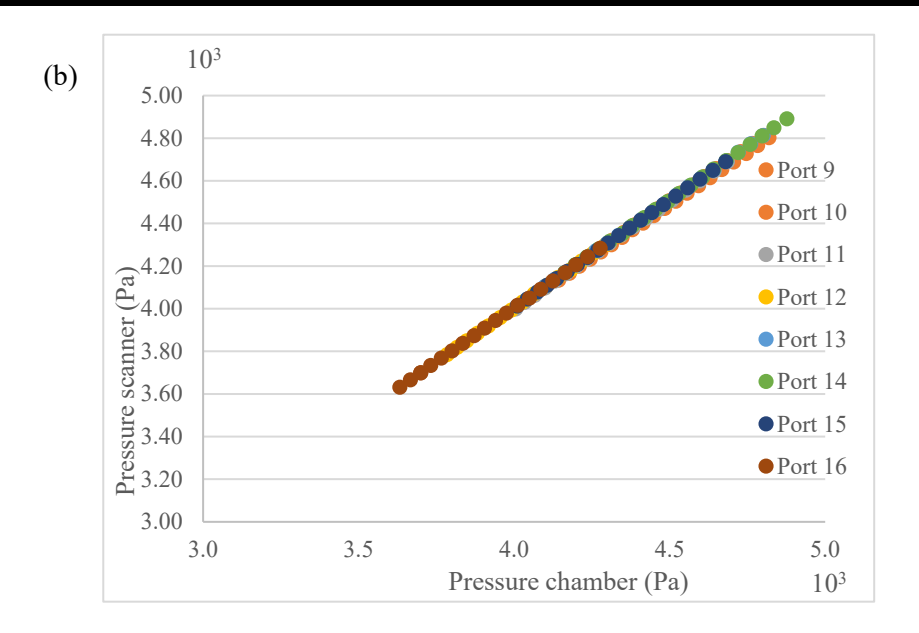


Figure 10: Pressure calibration results

# **4.2 Flow Velocity**

Figure 11 below shows the relationship between the wind speed values and frequency in between 11 m/s to 33 m/s. As the fan frequency of the wind tunnel increase, the wind tunnel speed increases. The relationship between two variables is about 0.9994 based on the R<sup>2</sup> value as shown below.

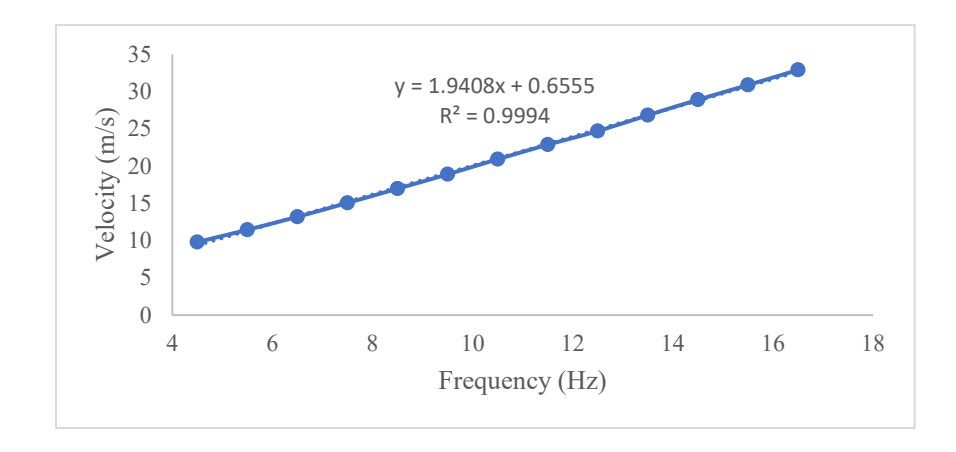
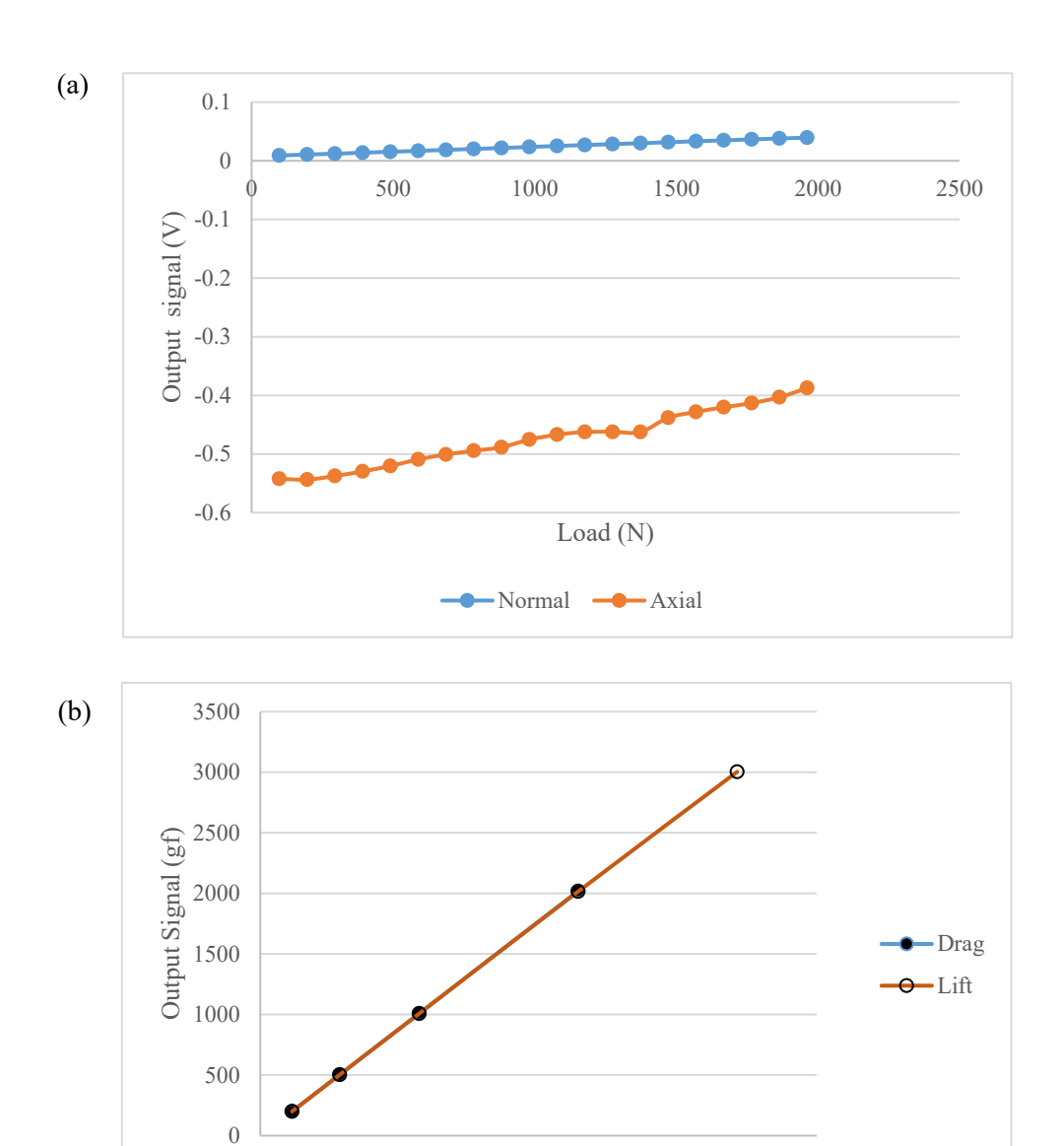


Figure 11: Wind speed calibration results

## 4.3 Force Balance

The relationship between the output signal and calibrated load for three-component force balance and sting balance is shown in Figure 12. Based on Figure 12, the linear slope between the applied load and output signal is noticeable for both force balances. This finding is similar to that of Abolezz et al. [28], who showed a linear increase in the output signal with respect to the applied force.





**Figure 12:** Normal and axial calibration graph for (a) five-components and (b) three-components balance

1500

2000

Load (gf)

2500

3000

3500

500

1000

# 4.4 Angle of Attack

To measure the angle of attack, mini digital protractor is used to identify the desired angle. The output signal generated from LabView was compared with the measured angle. The result is shown in Figure 13 and the finding supports the previous work from Abolezz et al [28].



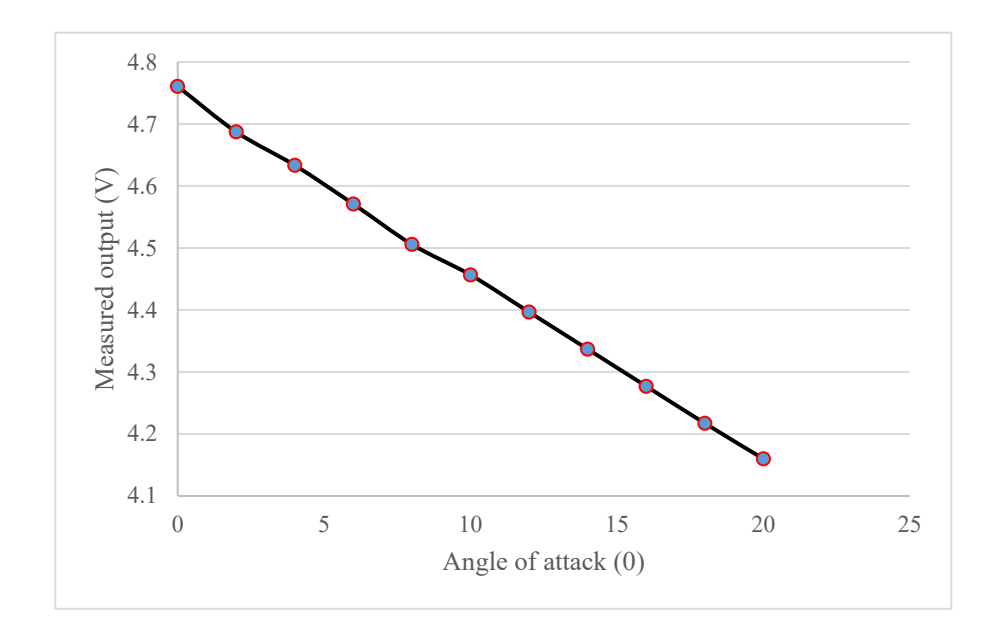
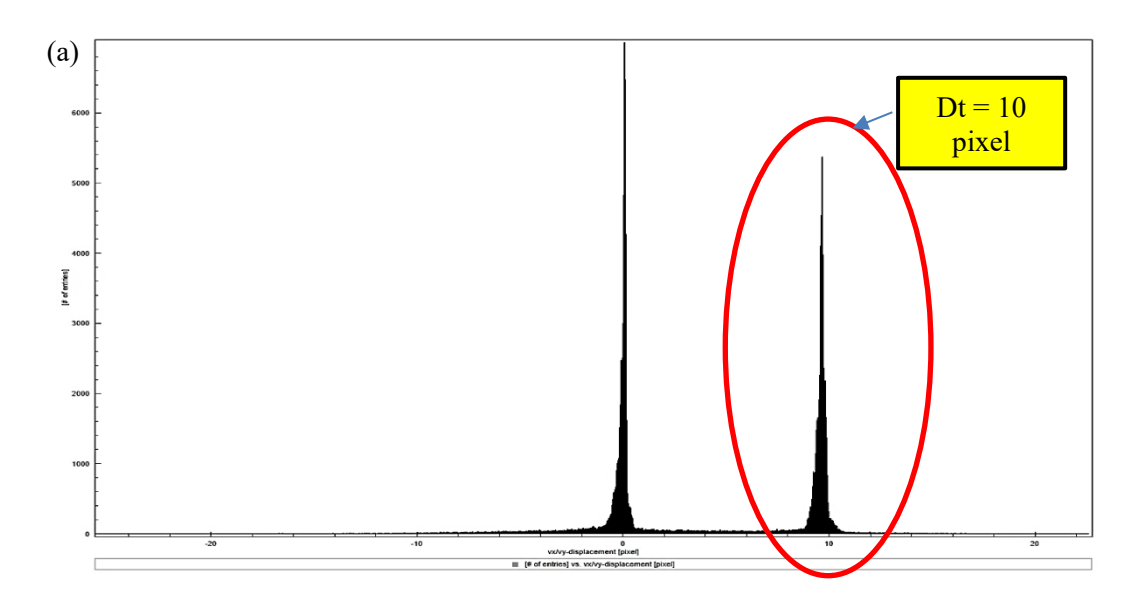


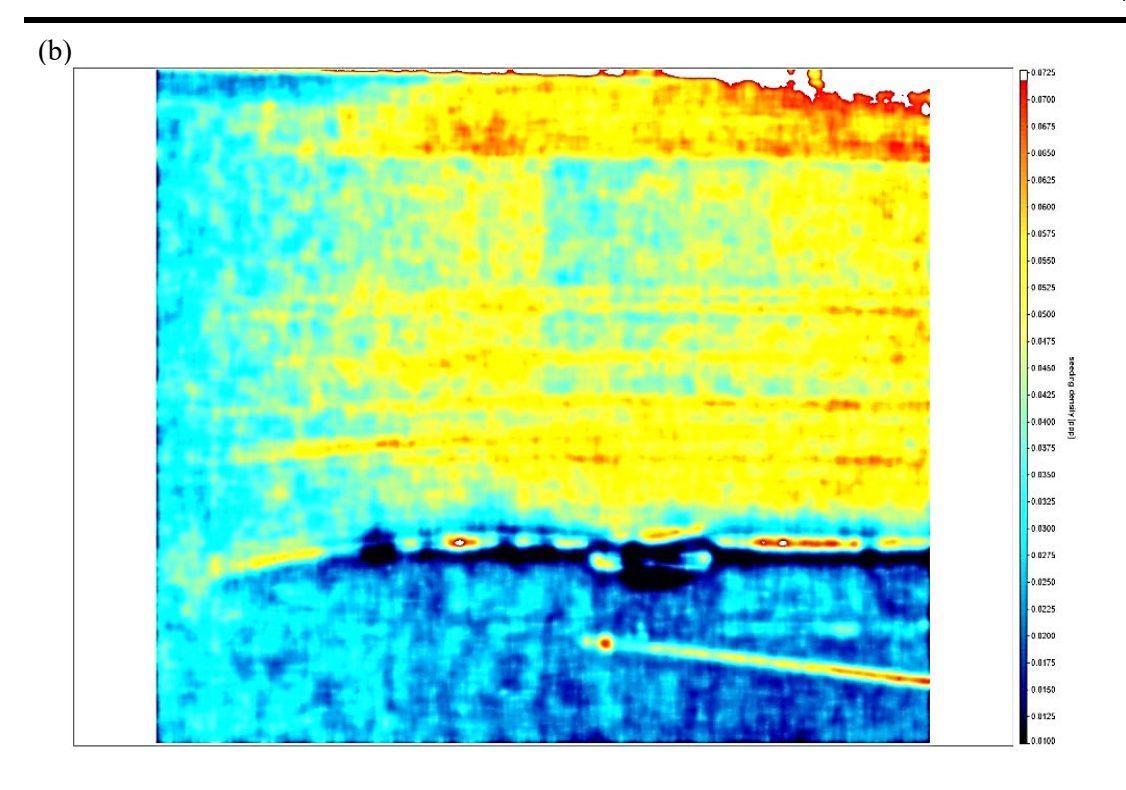
Figure 13: Angle of attack calibration results

# 4.5 Particle Image Velocimetry (PIV) Results

Following the calibration method requirement for PIV in section 3.4 to quantify the velocity field, the seeding particles manages to generate great flow imaging as shown in Figure 14.







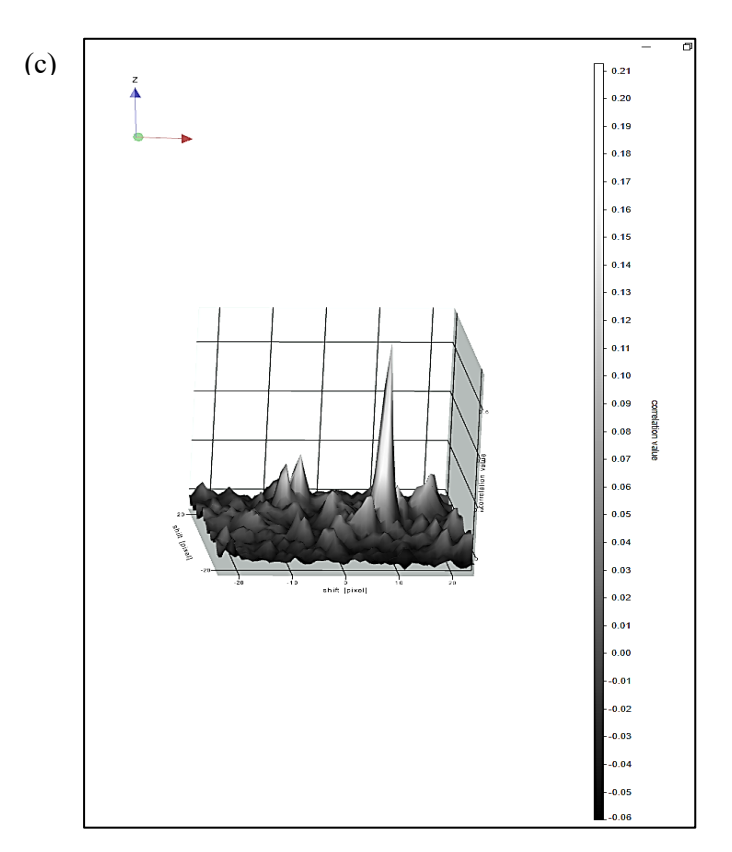


Figure 14: PIV calibration results



Based on Figure 14, the range of seeding particles for dt, seeding density (ppp) and correlation value range are considered acceptable. The time delay between two consecutive image frames in (a) is 10-pixel, the particle density in (b) is below 0.05 and the correlation value in (c) manages to produce one peak within the search area with medium multi-pass window size of 48 x 48. These seeding particles range is similar to the previous literature [35].

### 5.0 TURBULENT INTENSITY

The wall of the test section significantly affects the flow stream. The worst case is when the flow goes further down, the boundary layer of the wall test section increases thus reducing the effective area in the test section. However, previous study indicated that the turbulent intensity below 10% is falls within the acceptable range, thus the effect can be negligible [36]. Turbulent intensity (TI) is defined as the ratio of standard deviation of fluctuating velocity ( $\sigma$ ) to root mean square of the wind speed (Vrms) and the relation can be defined as equation 2 below.

$$TI = \frac{\sigma}{V_{rms}} \tag{2}$$

TI was obtained using similar method of finding flow velocity in the wind tunnel to gain the Vrms. The test was conducted at 3 different locations: frontal, middle and back field in the test section with low speed and high speed. The velocity mapping for each location was shown in Figure 15.

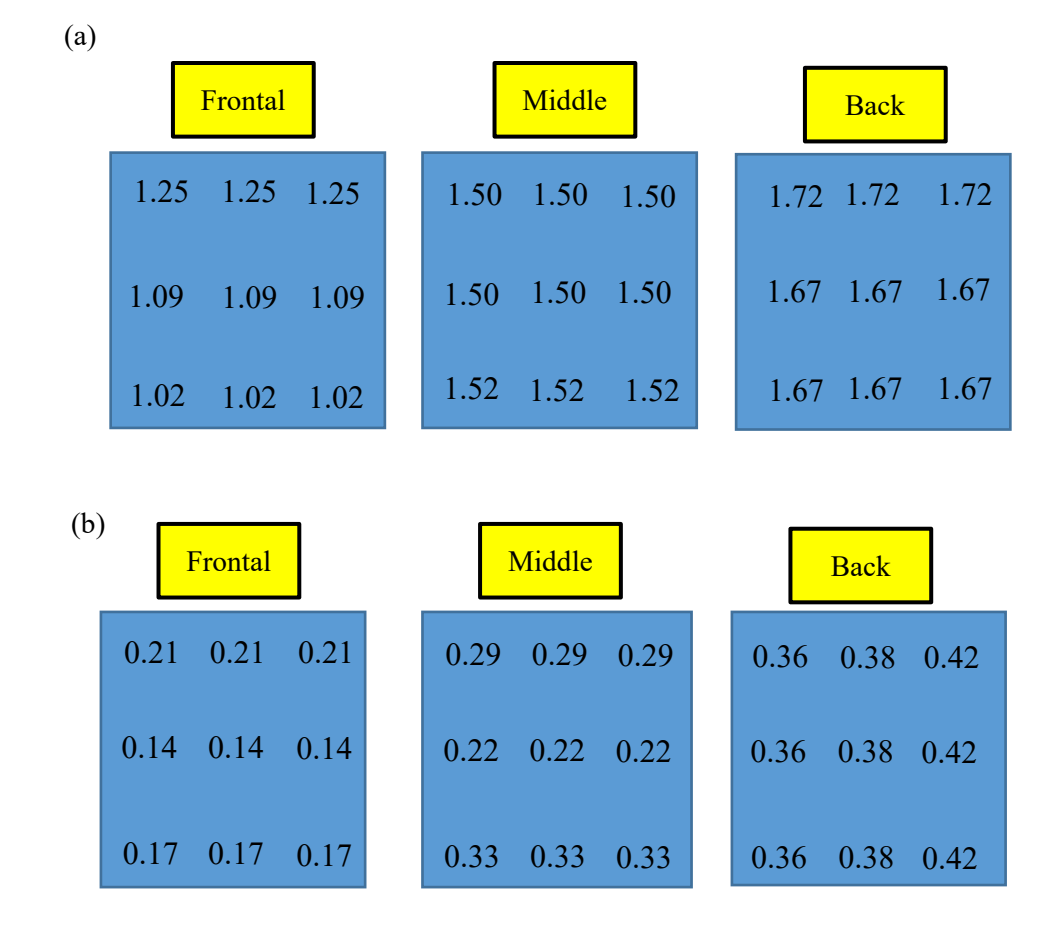




**Figure 15:** Turbulent intensity measurement at (a) low wind speed and (b) high wind speed in the test section

From Figure 15, it is apparent that the range of turbulent intensity increases as the flow travels down in the test section. This finding is similar to the finding of Ikarashi et al [37]. For low wind speed, the TI average at the frontal, middle and back field of the test section are 1.125%, 1.513% and 1.690% respectively. Meanwhile, for high wind speed, the average TI is relatively low compared to the low wind speed with an average of 0.177%, 0.282% and 0.393% for each area. From these results, it can be concluded that the wind tunnel has low turbulent intensity considering the measurement range is below than 10%. Therefore, the effect of TI due to the boundary layer wall can be negligible.

#### 6.0 CONCLUSION

A detailed calibration method for the pressure scanner (Scanivalve), force balance, and PIV has been completed for the UPNM Subsonic Wind Tunnel Facility. Ideally, the calibration should be performed before the experiment is conducted. This laborious and time-consuming procedure is necessary to ensure the accuracy of the collected data. During testing, a large number of samples were taken to reduce the measurement error due to line noise, temperature variations, and other experimental factors, as this variable has the greatest impact on the overall results. The accuracy for pressure measurement using Scanivalve is  $\pm 0.9\%$ . The relationship between the wind speed and frequency is 0.9994. The seeding particles falls within the acceptable range for a good visualization. The wind tunnel formed a uniform velocity profile and low turbulence intensity which is below 10%. This article documents the technique used for calibration, including turbulent intensity, that will be used for future reference in the UPNM Wind Tunnel Facility.

## Acknowledgement

This research was supported by the Ministry of Higher Education (MOHE) through the funding from UPNM/STFC-NEWTON/2018/TK/01. The authors also want to thank Universiti Pertahanan Nasional Malaysia (UPNM) for sponsoring the project through Graduate Research Assistant Fellowship under PPPI Trust Fund UPNM.

#### REFERENCES

- [1] Wang, L., Martin, J. E., Felli, M., and Carrica, P. M. (2020). Experiments and CFD for the propeller wake of a generic submarine operating near the surface. *Ocean Eng.*, 206, 107304
- [2] Houben, J. J. H., Weiss, C., Brunnmair, E., and Pirker, S. (2016). CFD simulations of pressure drop and velocity field in a cyclone separator with central vortex stabilization rod. *J. Appl. Fluid Mech.*, 9(1), 487–499



- [3] Wang, Z., and Liu, M. (2020). Semi-resolved CFD–DEM for thermal particulate flows with applications to fluidized beds. *Int. J. Heat Mass Transf.*, 159, 120150
- [4] Guzmán, C.H. *et al.* (2019). Implementation of virtual sensors for monitoring temperature in greenhouses using CFD and control. *Sensors (Switzerland)*, 19(1)
- [5] Liu, Y., et al. (2019). A CNN-based shock detection method in flow visualization. (2019). Comput. Fluids, 184, 1-9
- [6] Shen, R., Jiao, Z., Parker, T., Sun, Y., and Wang, Q. (2020). Recent application of Computational Fluid Dynamics (CFD) in process safety and loss prevention: A review. *J. Loss Prev. Process Ind.*, 67
- [7] Cattafesta, L., Bahr, C., and Mathew, J. (2010). Fundamentals of Wind-Tunnel Design. *Encycl. Aerosp. Eng*
- [8] Neverov, V. V., Kozhukhov, Y. V., Yablokov, A. M., and Lebedev, A. A. (2017). Optimization of a centrifugal compressor impeller using CFD: The choice of simulation model parameters. *IOP Conf. Ser. Mater. Sci. Eng.*, 232(1)
- [9] Van Breda, S. V., Vokalova, L., Neugebauer, C., Rossi, S. W., Hahn, S., and Hasler, P. (2019). Computational methodologies for the in vitro and in situ quantification of neutrophil extracellular traps. *Front. Immunol.*, 10,1–7
- [10] de Almeida, O., de Miranda, F. C., Ferreira Neto, O., and Saad, F. G. (2018). Low subsonic wind tunnel Design and construction. *J. Aerosp. Technol. Manag.*, 10, 1–20
- [11] Devisetty, H., P.M. C, Singh. D.B. (2021). Real-Time health monitoring system for Trisonic Wind Tunnel Nozzle. *International Journal of Advance Research and Innovative Ideas in Education.*, 7(4), 2395-4396
- [12] Namirian, Z., Mathure, S., Thorat, B., and Khetree, P. S. (2021). Modeling and Wind Flow Analysis of an Eiffel (Open) Type Sub-Sonic Wind Tunnel. *Glob. J. Res. Eng.*, 21(1),41–101
- [13] Seddik, A., Ahmed, M., Ayman, M., and Guaily, A. (2019). Design and Numerical Analysis of an Open-Circuit Low-Speed Wind Tunnel. *NILES 2019 Nov. Intell. Lead. Emerg. Sci. Conf.*, 71–75
- [14] Montazeri, H. (2011). Experimental and numerical study on natural ventilation performance of various multi-opening wind catchers. *Build. Environ.*, 46(2), 370–378
- [15] Shim, H. J., and Park, S. O. (2013). Low-speed wind-tunnel test results of a BWB-UCAV model. *Procedia Eng.*, 67, 50–58
- [16] Celis, B., and Ubbens, H. H. (2016). Design and Construction of an Open-circuit Wind Tunnel with Specific Measurement Equipment for Cycling," *Procedia Eng.*, 147, 98–



103

- [17] Rae, W. H., and Pope, A. (1954). Wind Tunnels, 7(8)
- [18] Ning, Z., and Hu, H. (2017). An experimental study on the aerodynamic and aeroacoustic performances of a bio-inspired UAV propeller. 35th AIAA Appl. Aerodyn. Conf.
- [19] Winslow, J., Otsuka, H., Govindarajan, B., and Chopra, I. (2018). Basic understanding of airfoil characteristics at low Reynolds numbers (104–105)," *J. Aircr.*, 55(3),1050–1061
- [20] Jumahadi, M. T., Saad, M. R., Idris, A. C., Sujipto, S., and Rahman, M. R. A. (2018). The potential of hybrid micro-vortex generators to control flow separation of NACA 4415 airfoil in subsonic flow. *AIP Conf. Proc.*, 1930
- [21] Baljit, S. S., Saad, M. R., Nasib, A. Z., Sani, A., Rahman, M. R. A., and Idris, A. C. (2017). Suction and Blowing Flow Control on Airfoil for Drag Reduction in Subsonic Flow. *J. Ph ys. Conf. Ser.*, 914(1), 1–8
- [22] Felli, M. (2020). Underlying mechanisms of propeller wake interaction with a wing. *J. Fluid Mech*
- [23] Ananda, G. K., Selig, M. S., and Deters, R. W. (2018). Experiments of propeller-induced flow effects on a low-Reynolds-number wing. *AIAA J.*, 56(8),3279–3294
- [24] Thomai, M. P., Sivamani, S., and Venkatesan, H. (2020). Dataset on the measurement of power in the hybrid vertical axis wind turbine in natural wind. *Data Br.*, 31,105922
- [25] Damak, A., Driss, Z., and Abid, M. S. (2017). Optimization of the helical Savonius rotor through wind tunnel experiments. *J. Wind Eng. Ind. Aerodyn.*, 174, 80–93
- [26] Xu, Y. L., Peng, Y. X., and Zhan, S. (2019). Variable pitch to high-solidity straight-bladed VAWTs for power enhancement. *Energy Procedia*, 158, 382–387
- [27] Kothe, L. B., Möller, S. V., and Petry, A. P. (2020). Numerical and experimental study of a helical Savonius wind turbine and a comparison with a two-stage Savonius turbine. *Renew. Energy*,148, 627–638
- [28] Aboelezz, A., Elqudsi, Y., Hassanalian, M., and Desoki, A. (2020). Wind tunnel calibration, corrections and experimental validation for fixed-wing micro air vehicles measurements. *Aviation*, 23(4),104–113
- [29] Balabajew, M., Van Engers, C. D., and Perkin, S. (2017). Contact-free calibration of an asymmetric multi-layer interferometer for the surface force balance. *Rev. Sci. Instrum.*, 88(12)



- [30] Neriya Hegade, K. P., Natalia, R., Wehba, B., Mittal, A., Bhat, R. B., and Packirisamy, M. (2020). Design and study of mini wind tunnel for microsystems fluid interaction under low Reynolds number flows. *SN Appl. Sci.*, 2(5), 1–14
- [31] Kumara, W. A. S., Elseth, G., Halvorsen, B. M., and Melaaen, M. C. (2010). Comparison of Particle Image Velocimetry and Laser Doppler Anemometry measurement methods applied to the oil-water flow in horizontal pipe. *Flow Meas. Instrum.*, 21(2),105–117
- [32] Nguyen, T., and Hassan,Y. (2017). Stereoscopic particle image velocimetry measurements of flow in a rod bundle with a spacer grid and mixing vanes at a low Reynolds number. *Int. J. Heat Fluid Flow*, 67, 202–219
- [33] Shi, S., Ding, J., Atkinson, C., Soria, J., and New, T. H. (2018). A detailed comparison of single-camera light-field piv and tomographic piv. *Exp. Fluids*, 59(3),1–13
- [34] Scharnowski, S., Grayson, K., de Silva, C. M., Hutchins, N., Marusic, I., and Kähler, C. J. (2017). Generalization of the PIV loss-of-correlation formula introduced by Keane and Adrian. *Exp. Fluids*, 8(10),1–12
- [35] Hadad, R. G. T. (2013). Characteristics of seeding particles for PIV / PTV analysis. Exp. Therm. Fluid Sci. 45 203–212, 203–213
- [36] Zhang, Y., Zhou, Z., Wang, and Li, X. (2020). Aerodynamic characteristics of different airfoils under varied turbulence intensities at low Reynolds numbers. *Appl. Sci.*, 10(5)
- [37] Ikarashi, Y., Uno, T., Yamagata, T., and Fujisawa, N. (2018). Influence of elbow curvature on flow and turbulence structure through a 90° elbow. *Nucl. Eng. Des.*, 339, 181–193